Influence of severe plastic deformation on dynamic strain aging of ultrafine grained Al–Mg alloys

Shiteng Zhao, Chenlu Meng, Fengxin Mao, Weiping Hu [*], Günter Gottstein

Institute of Physical Metallurgy and Metal Physics, RWTH Aachen University, Kopernikus Strasse 14, 52056 Aachen, Germany

Abstract

This investigation addressed the influence of severe plastic deformation (SPD) on dynamic strain aging (DSA) of ultrafine grained (UFG) Al–Mg alloys with different Mg content. Confined channel die pressing (CCDP) carried out at room temperature was used for SPD. Microcharacterization by TEM revealed a remarkable grain refinement and retarded dynamic recovery with increasing Mg content and plastic strain during SPD. Mechanical tests with jumping and constant strain rates demonstrated a complicated deformation behaviors of the UFG Al–Mg alloys: (i) the critical strain ε_c for initiation of serrated flow increased considerably with increasing strain and Mg content contrary to the behavior of the coarse grained and non-deformed counterparts; (ii) the instantaneous stress response ($\Delta\sigma_i$) and the instantaneous strain rate sensitivity (m_i) during rate jumps were always positive and increased monotonically with CCDP pass and Mg content, however, they exhibited a distinctive asymmetry with respect to the strain rate jump direction, i.e. the values for strain rate towards down were about one order of magnitude larger than those for rate towards up and increased with progressing CCDP as well as with increasing Mg content; (iii) the steady state strain rate sensitivity m_s was negative and decreased firstly with progressing CCDP up to a certain strain and then increased again. This mechanical behavior of UFG Al–Mg alloys is discussed on the basis of recently developed DSA models by relating the microstructure evolution of Al–Mg alloys during SPD to the influence of SPD on DSA.
© 2014 Acta Materialia Inc. Published by Elsevier Ltd. All rights reserved.

1. Introduction

Severe plastic deformation (SPD) has been widely used to fabricate bulk NC and UFG metallic alloys with remarkably higher strength and improved ductility for structural applications at low and moderate temperatures. It is therefore of particular interest to explore how SPD will impact dynamic strain aging (DSA) and thus, the deformation behavior and mechanical performance of as-fabricated UFG parts. On the one hand, it is expected that the extremely high defect (dislocation and vacancy) density due to the large plastic strain, high grain boundary volume fraction due to the intensive grain refinement and

deformation-induced precipitation or precipitate dissolution will affect DSA. On the other hand, DSA also strongly affects the strain hardening capability and hence, the plasticity/ductility and finally the mechanical properties of UFG alloys. Previous studies into these subjects have not provided useful theoretical guidance to a systematic utilization of UFG materials.

Serrated flow (or Portevin-Le Chatelier (PLC) effect), caused by dynamic strain aging (DSA) of solutes, leads to unstable yielding and flow that strongly affects material fabrication by plastic deformation. For this reason, many investigations on these phenomena have been carried out since the 1950s.

Cottrell was the first to propose an interaction of quasi-viscous moving dislocations with a solute atmosphere (or cloud) to interpret serrated yielding and jerky

* Corresponding author. Tel.: +49 241 8026869; fax: +49 241 8022301.
  E-mail address: hu@imm.rwth-aachen.de (W. Hu).

Nomenclature

A	material related constant
b	Burgers vector
$C(t_a, C_0)$	aging solute concentration
C_0	original alloy composition
C_∞	saturated aging concentration
C_v	vacancy concentration
d	grain size
D_0	diffusion pre-exponential factor
$\Delta E(t_a)$	binding energy between solutes and dislocation core
ΔE_∞^{core}	saturated binding energy
ΔG	Gibbs free energy of plastic deformation
k	Boltzmann constant
K	vacancy concentration prefactor
l_f	forest dislocation spacing
m	strain rate sensitivity
m_i	instantaneous strain rate sensitivity
m_s	steady state strain rate sensitivity
N	dislocation density prefactor
Q_m	effective activation energy for solute migration
r_{sol}	effective radius of solute atmosphere
r'_{sol}	solute atomic radius
T	absolute temperature
t_a	aging time of dislocations
t_d	intrinsic cross-core solute diffusion time
t_t	transition time
t_w	waiting time of dislocations in front of obstacles
V^*	activation volume
α	vacancy concentration exponent

β	dislocation density exponent
$\dot{\varepsilon}$	strain rate
$\dot{\varepsilon}_0$	strain rate pre-exponential factor
ε_c	critical strain for the onset of serrated flow
ρ	dislocation density
ρ_m	mobile dislocation density
ρ_f	forest dislocation density
σ	flow stress
$\sigma_{0.2}$	yield stress
σ_{th}	thermal stress component
σ_a	athermal stress component
σ_{DSA}	extra flow stress component contributed by dynamic strain aging
σ_{drop}	magnitude of stress drop during serrated flow
$\Delta\sigma_i$	instantaneous stress response upon strain rate jump
$\Delta\sigma_S$	steady state stress response
$\Delta\sigma_{th}$	change of thermal stress component upon strain rate jump
Ω	elementary strain
CCDP	confined channel die pressing
CG	coarse grained
DSA	dynamic strain aging
GB	grain boundary
PLC	Portevin-Le Chatelier
SPD	severe plastic deformation
SRS	strain rate sensitivity
nSRS	negative strain rate sensitivity
UFG	ultrafine-grained

flow as observed in steels and Al alloys during plastic deformation [1,2]. It is now generally accepted that serrated flow during plastic deformation of alloys is caused by DSA owing to the fact that solutes move to obstacles (e.g. junctions of forest and mobile dislocations) which block mobile dislocations via pipe and cross core diffusion and consequently, increase obstacle strength which further strengthens the material by increasing the activation stress of dislocation motion. The increased stress, thereby, enables mobile dislocations to break away from obstacle and to move freely until they meet the next obstacle [3,4]. DSA usually leads to a negative strain rate sensitivity (nSRS) of the alloy and makes itself felt by the PLC effect.

Van den Beukel et al. proposed vacancy-assisted models [4–7] for interpreting the onset of serrated yielding and the effect of DSA on SRS in Cu–Sn, Au–Cu and Al–Mg alloys. According to the vacancy-assisted model, DSA and the PLC effect were strain sensitive owing to the strain-dependent solute diffusivity and the strain dependent mobile dislocation density [6,7]. On the other hand, Kocks et al. proposed a strain hardening model incorporating pipe diffusion [8–10] based on the dislocation arrest theory

originally proposed by Sleeswyk [11]. In this case, the solute mobility will mainly influence the strain hardening component but not the friction component of the flow stress and therefore, DSA and the PLC effect should be stress sensitive but not strain sensitive [4].

Kubin and Estrin proposed a model to assess the critical conditions associated with the PLC effect which is based on the strain dependence of both the densities of mobile (ρ_m) and forest (ρ_f) dislocations but not on the deformation-induced vacancy density [12–15]. The occurrence of serrated flow owing to DSA and its disappearance due to dynamic recovery as well as the phenomenon of an inverse strain and temperature dependence of the PLC effect were predicted for CuMn and Al–Mg solid solutions by the model and showed qualitative agreement with experimental observations [16,17]. Recently, a constitutive model of the PLC effect was proposed by Rizzi and Hähner who described the spatial–temporal dynamics of the PLC effect by analyzing the evolution of an additional activation enthalpy during DSA owing to solute clustering at a dislocation junction [18,19]. Moreover, based on a statistical theory of coupled dynamics between mobile dislocations

and solutes, the relaxation effects due to DSA and the critical conditions for the PLC effect were also quantitatively analyzed [20]. Soare and Curtin investigated DSA in fcc metals based on the co-existence of solution strengthening/forest dislocation strengthening and solute aging at both mobile and forest dislocations through cross core diffusion [3,21]. In the model the binding energy between solutes and dislocations during cross core diffusion and the corresponding strength increment caused by dynamic aging were derived [21,22]. With a kinetic model based on a full thermal activation rate theory, the instantaneous and transition mechanical behavior of Al–Mg alloys due to DSA at rate jumps were analyzed [21]. Besides, a series of atomistic simulations was carried out by Picu et al. [23–25] for quantitatively assessing the influence of vacancies and dislocations on DSA and the PLC effect in fcc solid solutions. Moreover, the mechanisms for the normal and inverse behavior of the critical strain (ε_c) in plastically deforming Al–Mg alloys at different temperatures were proposed by Fu et al. [26]. An analytical model was also reported recently to predict the influence of strain rate and deformation temperature on the critical strain for the PLC effect [27].

Up to now, almost all investigations into DSA and the PLC-effect were conducted on coarse-grained (CG) materials. Reports of studies on DSA and PLC-effect in NC and UFG alloys, especially those produced by SPD, are relatively scarce and even contradictory. Kapoor et al. studied the mechanical behavior of an UFG Al–1.5Mg alloy subjected to ECAP [28,29]. They reported a shift of the nSRS domain towards the lower temperature range in as-ECAPed alloys compared to as-annealed coarse-grained alloys and a complex influence of annealing and deformation temperature on DSA and the PLC effect in as-ECAPed Al–Mg alloys. An investigation of the deformation kinetics of CG and as-ECAPed UFG commercially pure Ti reported quantitatively a more difficult break-away of mobile dislocations from solute clusters in UFG Ti compared to the CG counterpart. This was associated with the refined grain size and the dislocation structure leading to a lower initial effective stress and a limited dislocation mean free path [30].

Therefore, the purpose of the present investigation was to explore the influence of SPD processing, such as confined channel-die pressing (CCDP), on DSA of UFG Al–Mg alloys. This topic derives from the result that Al–Mg alloys do not promote superplastic deformation upon grain refinement owing to retention of a low strain rate sensitivity, which is attributed to DSA. Thus in particular, the DSA effect at room temperature under various conditions, i.e. Mg content, strain rate, and SPD strain, will be systematically investigated.

2. Experimental procedure

The Al–Mg alloys used in the present investigation had a magnesium content of 0.5%, 1%, 1.5%, 2%, 4%, and 5%

(all in wt.%), respectively, and in following theses alloys will be denoted as Al–0.5Mg,...5Mg, and so on. The alloys were prepared by melt processing using aluminum and magnesium with a purity of better than 4*N*. The cast ingot was solution annealed at 470 °C for 24 h followed by a quench in ice water. This annealing temperature is a little higher than 450 °C which corresponds to the largest solubility of Mg in Al (18 wt.%). After such heat treatment, Mg was in supersaturated solid solution without detectable precipitation even in Al–5Mg, as evidenced subsequently by TEM observations (see Fig. 3b). Therefore, all Al–Mg alloys prepared in the present investigation were actually in a solid solution state.

The samples for confined channel die pressing (CCDP) were cut from the as-heat treated Al–Mg ingots with a dimension of $9 \times 9 \times 12$ mm^3. CCDP was carried out with route II at RT for 1, 3, 6, 9, 12, 15 and 18 passes, respectively denoted as P1, P2,...P18, and so on, in the following. A detailed description of CCDP processing can be found elsewhere [31]. The specimens for mechanical testing and TEM observations were taken from the central volume ($3 \times 3 \times 3$ mm^3) of as-CCDPed samples where the equivalent strain ε after each pass of CCDP was $0.7 \leqslant \varepsilon \leqslant 1$, depending upon location from the border to the center of the volume [32].

The microstructure that evolved during CCDP was characterized by TEM. TEM foils with 3 mm diameter and about 0.1 mm thickness were taken from the central area of as-CCDPed cuboids along the TD direction of the last CCDP pass and double jet-polished in a TenuPol5 with an electrolytic solution of 938 ml methanol + 50 ml H$_2$SO$_4$ + 12 ml HF at -14 °C and 25–30 volt. The grain size as indicated by the boundary spacing (including cells, subgrains, and grains) was measured by dark field micrographs for more than 500 grains in each specimen. The misorientation evolution during CCDP was qualitatively analyzed by using selected area diffraction (SAD) patterns. The dislocation structures and the precipitation state were studied at high magnification.

The influence of SPD on deformation behavior of UFG Al–Mg alloys was investigated by mechanical testing at RT with both constant and jumping strain rates. For the constant strain rate tests, uniaxial tensile tests at $\dot{\varepsilon} = 5 \times 10^{-5}$ s^{-1}, $\dot{\varepsilon} = 1 \times 10^{-4}$ s^{-1} and $\dot{\varepsilon} = 1 \times 10^{-3}$ s^{-1} were conducted, respectively. The gauge volume was $3 \times 1.5 \times 1$ mm^3 with the tensile direction parallel to the long axis of as-CCDPed cuboids. The yield strength ($\sigma_{0.2}$), plastic elongation (ε) and critical strain (ε_c) at which serrated flow appeared were measured and determined by tensile tests with different constant strain rates.

Strain rate jump tests were carried out by compressing cylindrical samples ($\emptyset 1.5 \times 2.25$ mm^3) parallel to the long axis of as-CCDPed cuboids with alternate jumping rates between $\dot{\varepsilon} = 1 \times 10^{-4}$ s^{-1} (at strains of $\varepsilon = 3\%$ and 13%, respectively) and $\dot{\varepsilon} = 1 \times 10^{-3}$ s^{-1} (at $\varepsilon = 10\%$ and 19%, respectively). The strain rate sensitivity (SRS), including instantaneous (m_i) and steady state SRS (m_s), the flow

stress response ($\Delta\sigma$), including instantaneous ($\Delta\sigma_i$) and steady state ($\Delta\sigma_s$) changes at the rate jump as well as the transient time (t_t) that lasted during stress relaxation from the instantaneous response to steady state were evaluated by the strain rate jump tests. The definitions of m_i, m_s, $\Delta\sigma_i$, $\Delta\sigma_s$ and t_t are illustrated schematically in Fig. 1.

For the strain rate jump tests, an electromechanical testing machine (DZM) was used with a 12,500N load cell, which had an accuracy of better than ± 0.17 MPa in stress measurement. Given this accuracy, the mechanical behavior such as DSA/PLC effect and SRS of UFG Al–Mg alloys can be studied reliably. No stiffness or true strain rate corrections were applied in the evaluation of stress–strain curves and strain rate jump tests since for the objective of this study the respective effects were considered of second order.

3. Results

3.1. Microstructural characterization

The microstructure evolution of Al–Mg alloys with different Mg content during CCDP was investigated by TEM. The results taken from as-CCDPed Al–1Mg and Al–5Mg are shown in Fig. 2a and b. The measured grain size (including cells, subgrains and grains) of Al–1Mg, Al–2Mg and Al–5Mg are given in Fig. 2c as a function of CCDP pass number and Mg-content. It is seen that after 1 pass CCDP the microstructure of both Al–1Mg and Al–5Mg comprised mainly coarse grains elongated along the shear direction which were subdivided by non-uniformly distributed dislocation tangles (or cells) (see P1 of Fig. 2a and b), which is different from Al–Mg alloys subjected to only small or moderate plastic strain ($\varepsilon < 0.2$) where a uniform distribution of dislocation tangles is formed [33,34]. The grain size decreased not only with increasing SPD strain (or CCDP pass number) but also with larger Mg-content. In comparison to Al–1Mg where the grain size decreased from several hundred micrometers in non-deformed samples to about 250 nm after 12 passes, the grain size in Al–5Mg was refined to about 100 nm after

a similar deformation. However, the grain size decreased precipitously up to 6 to 9 passes, thereafter the rate of refinement leveled off (see Fig. 2c). The misorientation increased constantly during the whole CCDP process indicating a growing amount of high angle grain boundaries with rising SPD strain, as qualitatively manifested by SAD patterns (Fig. 2a and b). Furthermore, with increasing Mg-content the appearance of a stable microstructure was delayed to larger strains, e.g. after 9 CCDP passes the microstructure was mainly composed of subgrains and grains in Al–1Mg (Fig. 3a), indicating evident dynamic recovery, whereas the microstructure of Al–5Mg mainly contained dislocation cells of different cell wall thickness, revealing retarded dynamic recovery (Fig. 3b). This observation is consistent with the case of as-ECAPed Al–Mg alloy, as reported by Gubiza et al. [34] and Morris et al. [35].

No detectable precipitation was found in UFG Al–Mg alloys even in Al–5Mg (Fig. 3b). This means that strain-induced precipitation did not occur in the UFG Al–Mg alloys during CCDP and therefore, the Al–Mg alloys used in the present investigation were all in a solid solution state.

3.2. Mechanical behavior

3.2.1. Constant strain rate

The yield strength ($\sigma_{0.2}$) of Al–Mg alloys was measured by tensile tests at $\dot{\varepsilon} = 1 \times 10^{-4}$ s^{-1}. The yield strengths of Al–1Mg, Al–2Mg and Al–5Mg are summarized in Fig. 4 as function of CCDP pass number, revealing that $\sigma_{0.2}$ increased monotonically with progressive SPD as well as with rising Mg-content at the same CCDP strain.

The critical strain (ε_c) for serrated flow of Al–Mg alloys subjected to different CCDP was determined by tensile tests at $\dot{\varepsilon} = 1 \times 10^{-3}$ s^{-1}, 1×10^{-4} s^{-1} and 5×10^{-5} s^{-1}, respectively (Fig. 5). Fig. 5a shows the true stress – true strain curves at 1×10^{-4} s^{-1} taken from Al–1.5Mg subjected to different SPD strain. The data in Fig. 5b display a considerable fluctuation, especially those measured at 1×10^{-3} s^{-1}, since the small stress drop due to the relatively high strain rate became comparable to the stress
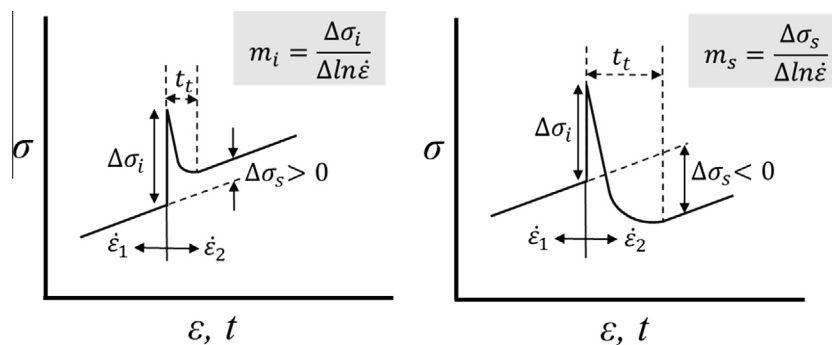

Fig. 1. Schematic illustration and definition of instantaneous and steady state stress responses $\Delta\sigma_i$ and $\Delta\sigma_s$, strain rate sensitivity m_i and m_s and transient time t_t at a strain rate-up jump, where $\dot{\varepsilon}_1 < \dot{\varepsilon}_2$ for $\Delta\sigma_s > 0$ (left figure) and $\Delta\sigma_s < 0$ (right figure).
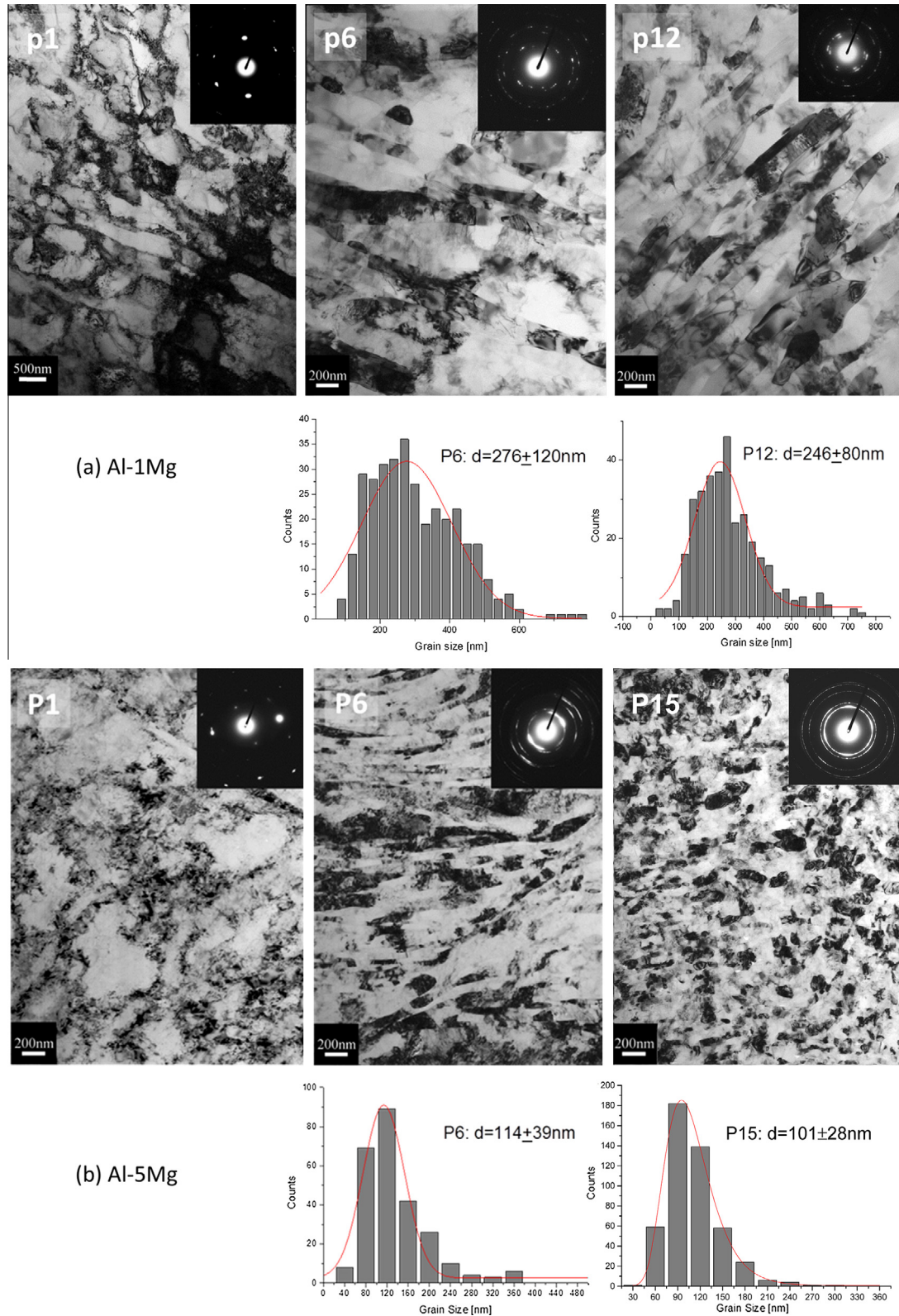
Fig. 2. Microstructure evolution in terms of TEM micrographs and grain size distributions during CCDP. (a) Al–1Mg after 1, 6 and 12 passes and (b) Al–5Mg after 1, 6 and 15 passes. (c) Mean grain size of Al–1Mg, Al–2Mg, Al–5Mg and pure Al with increasing number of CCDP passes.

fluctuation caused by the testing machine, so that ε_c could then not be exactly determined. However, a common tendency of ε_c during CCDP can still be seen, i.e. ε_c increased

apparently with increasing $\dot{\varepsilon}$ and also CCDP pass number (or SPD strain). Moreover, after 3 passes, ε_c grew also obviously with increasing Mg-content at the same SPD
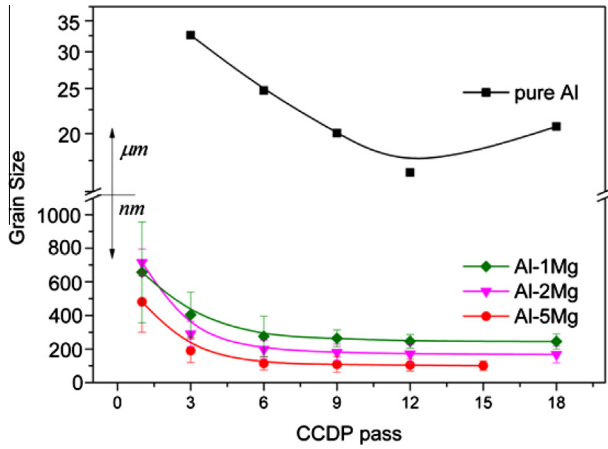
Fig 2. (continued)

which ε_c decreases with increasing solute concentration [5]. Furthermore, with smaller $\dot{\varepsilon}$ the growth rate and the scatter of ε_c decreased. For the applied experimental conditions no up-critical strain or inversed critical strain behavior was observed.

3.2.2. Strain rate jump tests

The mechanical behavior displayed by UFG Al–Mg alloys during strain rate jump tests can be classified into instantaneous and steady state behavior, as schematically illustrated in Fig. 1. The obtained behavior was found to be virtually independent of the strain prior to the jump tests so that a given set of values reflects the strain rate sensitivities for a particular material state (CCDP predeformation and chemical composition), i.e. for the entire hardening curve.

strain (Fig. 5b). This behavior is apparently contrary to that of coarse grained and non-deformed material, in

3.2.2.1. Instantaneous properties. The instantaneous stress response ($\Delta\sigma_i$), SRS (m_i) and the transient time (t_t) of
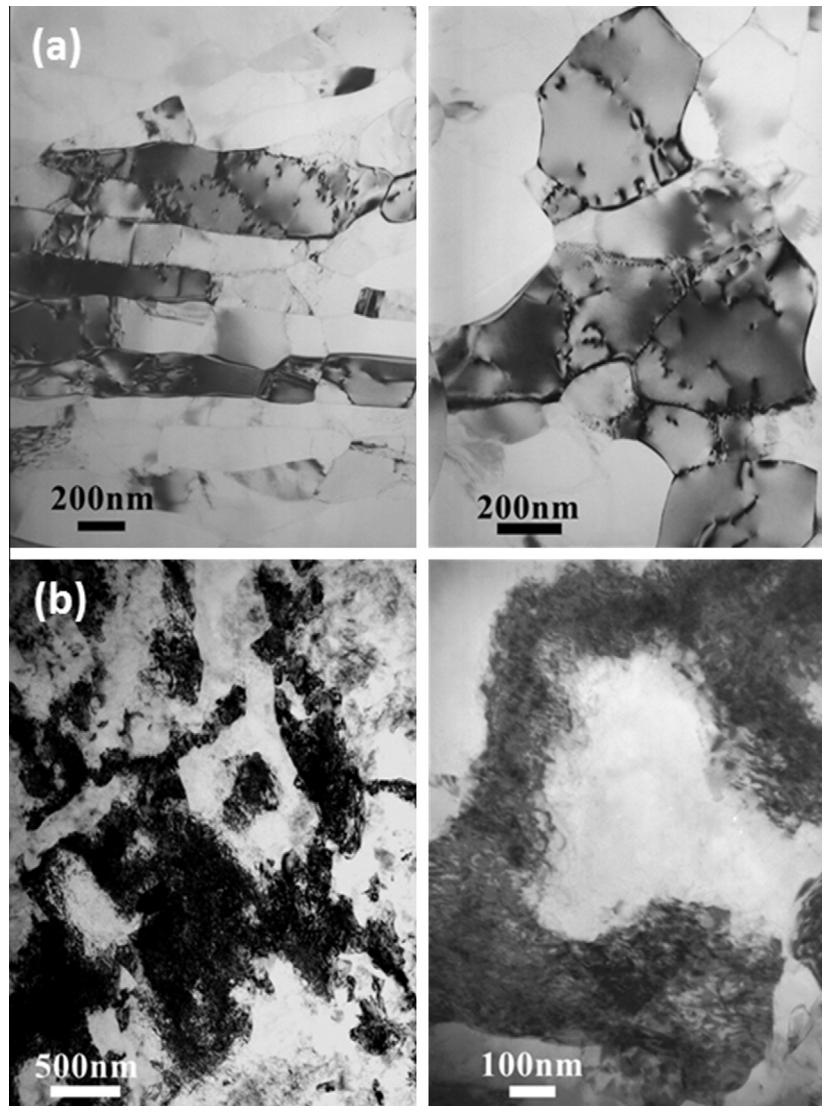

Fig. 3. TEM micrographs of UFG Al–Mg alloys. (a) Al–1Mg after 9 passes. (b) Al–5Mg after 9 passes (left figure) and 12 passes (right figure).
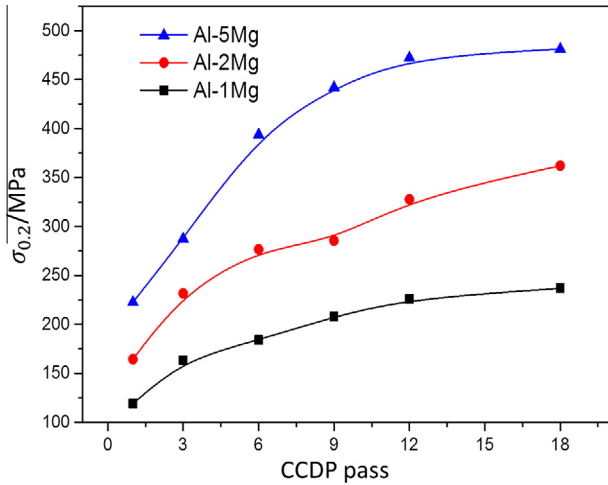
Fig. 4. Influence of CCDP pass number on 0.2% proof stress ($\sigma_{0.2}$) of Al–1Mg (bottom curve), Al–2Mg (center curve) and Al–5Mg (top curve).

Al–Mg alloys were measured by strain rate jump tests between 1×10^{-3} s^{-1} and 1×10^{-4} s^{-1}. Since the trend of those material parameters was similar and it was only gradually intensified by increasing Mg-content, only the results of two alloys, Al–1Mg and Al–5Mg are given here. Fig. 6a shows the true stress–true strain curves taken from double jump tests. For comparison, the corresponding data of pure Al without DSA which were obtained with the same preparation and testing procedures are also given in

Fig. 6a. The measured $\Delta\sigma_i$, m_i and t_t as a function of CCDP pass number are given in Fig. 6b and c for Al–1Mg and Fig. 6d and e for Al–5Mg. It is seen from Fig. 6a–e that the instantaneous $\Delta\sigma_i$ and m_i are always positive for the Al–Mg alloys. However, $\Delta\sigma_i$, m_i and t_t were not symmetrical with respect to rate towards down and towards up behavior: the values from the rate towards down tests were about one order of magnitude larger than those from the rate towards up tests (Fig. 6b–e). Furthermore, the influence of SPD on the instantaneous properties was also different for the rate-down and rate-up tests. The $\Delta\sigma_i$, m_i and t_t from rate-down tests increased substantially with increasing CCDP pass number. By contrast, however, the corresponding values from rate-up tests grew very little with pass number, i.e. SPD affected the instantaneous properties more strongly in rate-down than in rate-up tests. In addition, the influence of SPD on the asymmetry rose also with increasing Mg-content. By contrast, for pure Al, where DSA can be ignored, $\Delta\sigma_i$, m_i and t_t were roughly symmetrical for rate-down and rate-up tests, and changed merely with increasing CCDP pass numbers.

3.2.2.2. Steady state properties. Steady state stress response ($\Delta\sigma_s$) and SRS (m_s) of Al–Mg alloys measured in the current study were always negative, except for Al–0.5Mg after 18 passes (Fig. 7). Obviously, these negative and near zero values of $\Delta\sigma_s$ and m_s in UFG Al–Mg alloys resulted from DSA as common in Al–Mg alloys. Furthermore, the steady
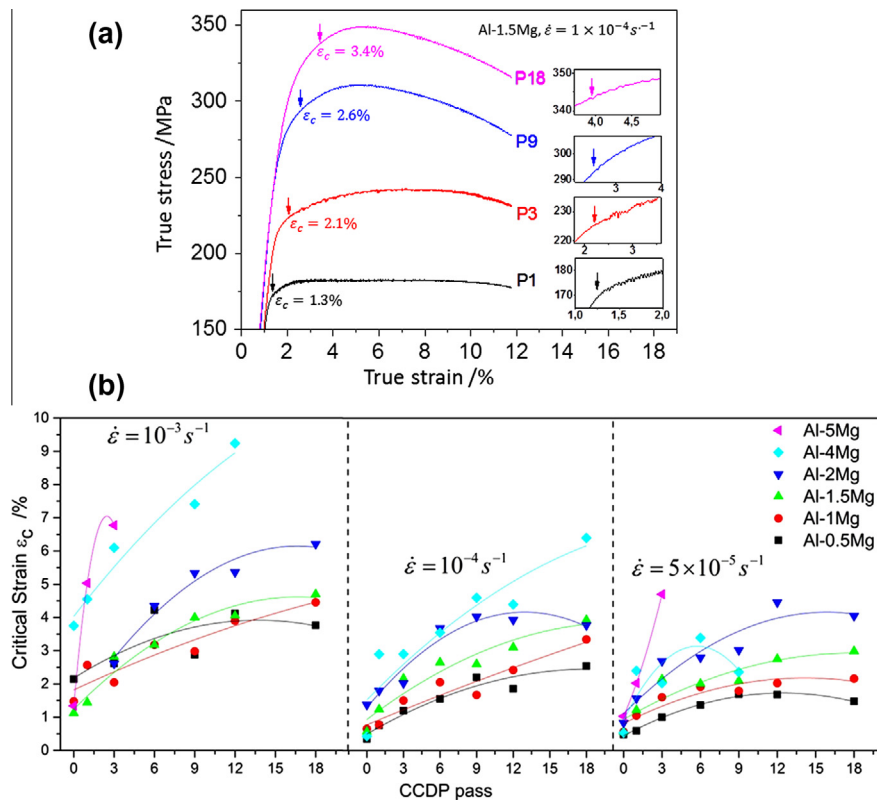

Fig. 5. (a) Tensile response of Al–1.5Mg at $\dot{\varepsilon} = 1 \times 10^{-4}$ s^{-1} subjected to CCDP. (b) influence of CCDP pass number, Mg-content, and strain rate on the critical strain (ε_c) for DSA of Al–Mg alloys (curves represent fits by 2nd order polynomials).
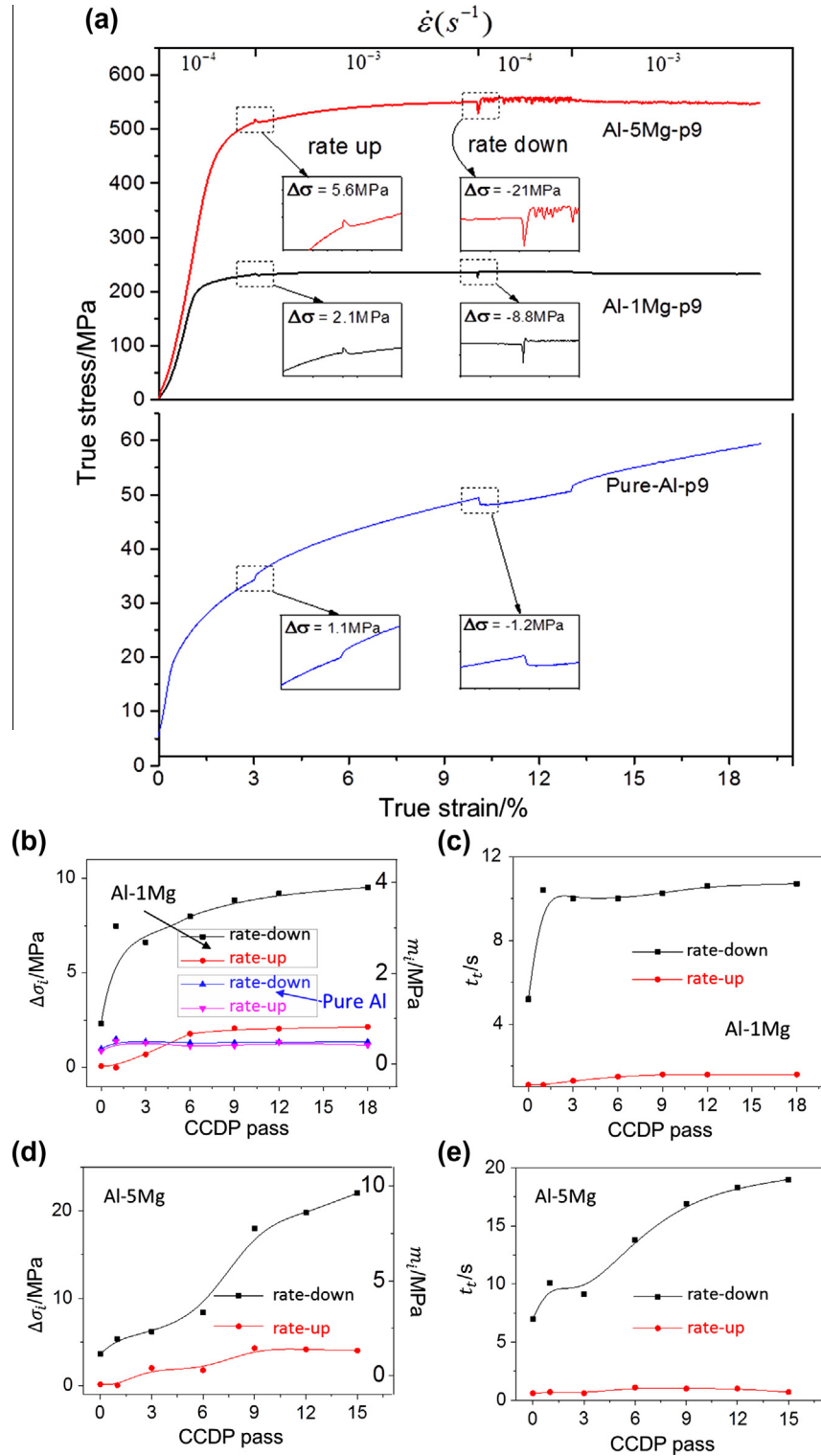
Fig. 6. Behavior of Al–Mg alloys during strain rate jump tests for increasing CCDP pass number. (a) Flow curve and local blow-up at the strain rate jump positions for Al–5Mg, Al–1Mg and pure Al, respectively. (b) $\Delta\sigma_i$ and m_i of Al–1Mg and pure Al. (c) t_t of Al–1Mg. (d) $\Delta\sigma_i$ and m_i of Al–5Mg, and (e) t_t of Al–5Mg. (see Fig. 1 for definitions).

state parameters $\Delta\sigma_s$ and m_s were not so sensitive to rate-up and rate-down jumps, i.e. no apparent differences were found between the values attained from both rate jump modes. Therefore, $\Delta\sigma_s$ and m_s of a specific sample were

converted to a mean value of all measured values from rate-down and rate-up tests at strains of 3%, 10%, 13% and 19%, respectively. The evolution of m_s (or $\Delta\sigma_s$) with respect to progressive SPD strain yielded a saddle-shape
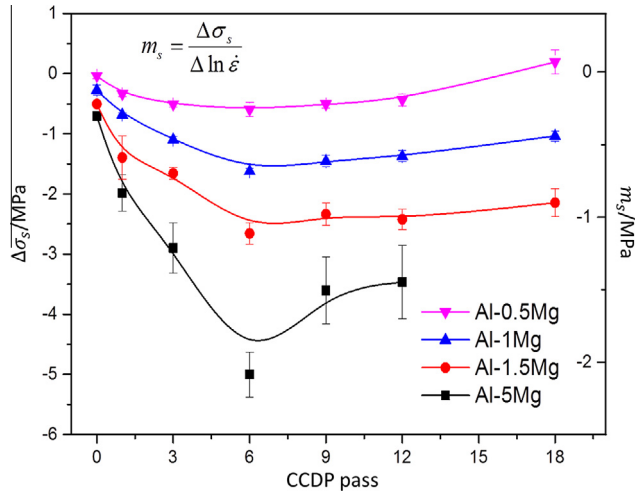
Fig. 7. Steady state stress response ($\Delta\sigma_s$) and corresponding strain rate sensitivity m_s as function of CCDP pass number for Al–Mg alloys with different Mg-content.

curve, as shown in Fig. 7, i.e. it decreased continuously up to 6 passes and then came back up. The larger the Mg-content, the stronger was the decrease and the bounce back of m_s.

The data of the current study were compared with results on extruded cryomilled commercial alloy AA5083 (4.6% Mg, 0.6% Mn and 0.1% Cr in wt. percent). Under similar conditions of strain and strain rate the UFG AA5083 alloy had an SRS of $m_i \approx 0.003 - 0.014$ and $m_s \approx -0.006$ to -0.01 at room temperature [36–38] which is comparable to the data obtained in the current investigation.

4. Discussion

4.1. Evolution of microstructure and flow stress during progressive SPD

Al–Mg alloys are a non-cell forming materials when deformed at small and/or medium strains (generally smaller than $\varepsilon < 20\%$). However, with increasing plastic strain ($\varepsilon > 20$–50%) the uniform distribution of dislocation tangles will be replaced by the formation of cellular substructures and domain boundaries due to shear offsets caused by microband intersection [33]. By severe plastic strain, e. g. by CCDP or ECAP, cells, subgrains and even grains will be formed by dynamic recovery [34,35]. This is why in the current study merely cells and subgrains rather than uniformly distributed dislocation tangles were observed even in the Al–Mg alloys just subjected to 1 pass of CCDP (see P1 of Fig. 2a and b where the equivalent strain is about 0.7–1). Increasing Mg content lowered the dynamic recovery rate and postponed the development of a stable microstructure to a large SPD strain (see P12 in Fig. 2b and Fig. 3) apparently due to pinning and slowing down mobile dislocations by hindering the annihilation of dislocations during deformation due to the interaction of Mg atoms with dislocations [34].

The yield stress of Al–Mg alloys increased with SPD strain (Fig. 4). This can be attributed to grain refinement as well as work hardening induced by the SPD process. However, grain refinement saturated after 6 passes of CCDP (Fig. 2c), whereas the yield strength continued to increase, although moderately. This may be due to (1) a continuous increase of misorientation (or increase of the fraction of high angle grain boundaries) during CCDP even though the grain refinement leveled off and (2) an enhancement of solid solution strengthening effect when the grain size decreased to a certain value, owing to an increasing effect of solute atoms on global material properties (shear modulus G and Burgers vector b) when grain size is remarkably reduced [39].

4.2. Transient asymmetry at rate-jump positions

In strain rate jump tests, the transition behavior exhibited distinct differences, depending on the direction of the rate jump, i.e. the instantaneous stress response $\Delta\sigma_i$, the instantaneous SRS m_i, and the transient time t_t were usually one order of magnitude larger for downwards transients than for upwards transients. Such transient asymmetry was strongly intensified by the CCDP process, and a quantitative analysis of which considering the effect of SPD on DSA will be presented in following.

In rate jump tests with alternating strain rates of $\dot\varepsilon_1$ and $\dot\varepsilon_2$, where $\dot\varepsilon_1 < \dot\varepsilon_2$ and the rate changing from $\dot\varepsilon_1$ to $\dot\varepsilon_2$ (upwards jump), the initial flow stress at $\dot\varepsilon_1$ can be expressed as

$$\sigma(\dot\varepsilon_1) = \sigma_{th}(\dot\varepsilon_1, T) + \sigma_a + \sigma_{DSA}(\dot\varepsilon_1, T, C(\dot\varepsilon_1, T,)) \quad (1)$$

where $\sigma_{th}(\dot\varepsilon_1, T)$ is the thermal stress component depending on strain rate $\dot\varepsilon$ and deformation temperature T, σ_a the athermal stress component that is weakly dependent on T and independent of $\dot\varepsilon$, and $\sigma_{DSA}(\dot\varepsilon_1, T, C(\dot\varepsilon_1, T,))$ a pinning stress exerted by solute atoms on mobile dislocations waiting in front of the forest obstacles (i.e. DSA effect). Apparently, $\sigma_{DSA}(\dot\varepsilon_1, T, C(\dot\varepsilon_1, T,))$ has not only the character of a thermal stress component due to short range interaction of mobile dislocations with pinning solute atoms at strain rate jump but also possesses a feature of an athermal stress component owing to the solute concentration $C(\dot\varepsilon_1, T,)$ at arrested mobile dislocations. Even though $C(\dot\varepsilon_1, T,)$ is a function of $\dot\varepsilon_1$ and T, it has a relationship with T and $\dot\varepsilon$ inverse to that of σ_{th}, i.e. a lower $\dot\varepsilon$ or higher T corresponds to a larger σ_{DSA} owing to the stronger solute aging on dislocations by solute diffusion. In the current study, the tests were carried out at RT, i.e. T was constant, thus, merely $\dot\varepsilon$ and C were the variables so that Eq. (1) can be rewritten as

$$\sigma(\dot\varepsilon_1) = \sigma_{th}(\dot\varepsilon_1) + \sigma_a + \sigma_{DSA}(\dot\varepsilon_1, C(\dot\varepsilon_1)) \quad (2)$$

At the moment of the strain rate upwards change from $\dot\varepsilon_1$ to $\dot\varepsilon_2$, the flow stress increases instantaneously to

$$\sigma(\dot\varepsilon_2) = \sigma_{th}(\dot\varepsilon_2) + \sigma_a + \sigma_{DSA}(\dot\varepsilon_2, C(\dot\varepsilon_1)) \quad (3)$$

where $C(\dot{\varepsilon}_1)$ remains at the state of $\dot{\varepsilon}_1$ since the aging solute concentration at arrested mobile dislocations does not change at the moment of strain rate jump due to the diffusion dependent (and thus, also time dependent) nature of the DSA effect. The instantaneous stress response $\Delta\sigma_i(up)$ is therefore

$$\begin{aligned}
\Delta\sigma_i(up) &= \sigma(\dot{\varepsilon}_2) - \sigma(\dot{\varepsilon}_1) = \sigma_{th}(\dot{\varepsilon}_2) - \sigma_{th}(\dot{\varepsilon}_1) \\
&\quad + \sigma_{DSA}(\dot{\varepsilon}_2, C(\dot{\varepsilon}_1)) - \sigma_{DSA}(\dot{\varepsilon}_1, C(\dot{\varepsilon}_1)) \\
&= \Delta\sigma_{th}(\dot{\varepsilon}_{2-1}) + \Delta\sigma_{DSA}(\dot{\varepsilon}_2 - \dot{\varepsilon}_1, C(\dot{\varepsilon}_1)) \\
&= \Delta\sigma_{th}(\dot{\varepsilon}_{2-1}) + \sigma'_{DSA}(C(\dot{\varepsilon}_1))
\end{aligned} \quad (4)$$

The instantaneous response of the thermal flow stress $\Delta(\sigma_{th}(\dot{\varepsilon}_{2-1})$ reflects the strain rate sensitivity of σ_{th} at constant dislocation structure at the moment of the strain rate change. The absolute value of $\sigma_{DSA}(\dot{\varepsilon}_2, C(\dot{\varepsilon}_1))$ is larger than that of $\sigma_{DSA}(\dot{\varepsilon}_1, C(\dot{\varepsilon}_1))$ due to the higher stress necessary to unpin the mobile dislocations from the solute atoms at the higher strain rate. The term $\sigma'_{DSA}(C(\dot{\varepsilon}_1) = \Delta\sigma_{DSA}(\dot{\varepsilon}_2 - \dot{\varepsilon}_1, C(\dot{\varepsilon}_1))$ is an effective (or net) pinning stress exerted by aging solute atoms on arrested mobile dislocations at the moment of strain rate change from $\dot{\varepsilon}_1$ to $\dot{\varepsilon}_2$. The magnitude and direction of $\Delta\sigma_i(up)$ are determined by the magnitude of $\Delta\sigma_{th}(\dot{\varepsilon}_{2-1})$ and $\sigma'_{DSA}(C(\dot{\varepsilon}_1))$. In the current study, the measured $\Delta\sigma_i(up)$ was always positive (see Fig. 6), i.e. $|\Delta\sigma_{th}(\dot{\varepsilon}_{2-1})| > |\sigma'_{DSA}(C(\dot{\varepsilon}_1))|$.

Along the same lines, the instantaneous stress response for strain rate downwards change can be expressed by

$$\begin{aligned}
\Delta\sigma_i(down) &= \sigma(\dot{\varepsilon}_1) - \sigma(\dot{\varepsilon}_2) \\
&= \sigma_{th}(\dot{\varepsilon}_1) - \sigma_{th}(\dot{\varepsilon}_2) + \sigma_{DSA}(\dot{\varepsilon}_1, C(\dot{\varepsilon}_2)) \\
&\quad - \sigma_{DSA}(\dot{\varepsilon}_2, C(\dot{\varepsilon}_2)) \\
&= \Delta\sigma_{th}(\dot{\varepsilon}_{1-2}) + \Delta\sigma_{DSA}(\dot{\varepsilon}_1 - \dot{\varepsilon}_2, C(\dot{\varepsilon}_2)) \\
&= \Delta\sigma_{th}(\dot{\varepsilon}_{1-2}) + \sigma'_{DSA}(C(\dot{\varepsilon}_2))
\end{aligned} \quad (5)$$

where $\Delta(\sigma_{th}(\dot{\varepsilon}_{1-2})$ corresponds to the thermally activated stress drop due to the decreased strain rate, and $\sigma'_{DSA}(\dot{\varepsilon}_2)$ denotes the effective solute pinning effect (or DSA effect) at the higher strain rate. Opposite to the strain rate upwards change, $\Delta\sigma_i(down)$ is negative and both $\Delta\sigma_{th}(\dot{\varepsilon}_{1-2})$ and $\sigma'_{DSA}(\dot{\varepsilon}_2)$ act in the same direction.

The extent of asymmetry of $\Delta\sigma_i$ between rate-up and rate-down jumps can be quantitatively evaluated by adding Eqs. (4), (5) in absolute terms

$$\begin{aligned}
|\Delta\sigma_i(up) + \Delta\sigma_i(down)| &= |\Delta\sigma_{th}(\dot{\varepsilon}_{2-1}) + \sigma'_{DSA}(\dot{\varepsilon}_1) \\
&\quad + \Delta\sigma_{th}(\dot{\varepsilon}_{1-2}) + \sigma'_{DSA}(\dot{\varepsilon}_2)| \\
&= |\sigma'_{DSA}(\dot{\varepsilon}_1) + \sigma'_{DSA}(\dot{\varepsilon}_2)|
\end{aligned} \quad (6)$$

where the thermal stress components $\Delta\sigma_{th}(\dot{\varepsilon}_{2-1})$ and $\Delta\sigma_{th}(\dot{\varepsilon}_{1-2})$ are considered equal in magnitude but opposite in sign. This assumption was validated by double-rate jump tests on DSA-free pure Al, where $\Delta\sigma_{th}$ for upwards and downwards transitions were approximately the same (Fig. 6a and b). Eq. (6) reveals the physical nature of the observed asymmetry in $\Delta\sigma_i$, namely the different magnitude of σ'_{DSA} at $\dot{\varepsilon}_1$ and $\dot{\varepsilon}_2$ gives rise to the asymmetry of $\Delta\sigma_i$. The

absolute value of $\Delta\sigma_i(down)$ was always larger than $\Delta\sigma_i(up)$. The difference between them is equal to the sum of the net pinning stress of solute atoms σ_{DSA} at different strain rates.

The evolution of the asymmetry of $\Delta\sigma_i$ (or the evolution of $|\sigma'_{DSA}(\dot{\varepsilon}_1) + \sigma'_{DSA}(\dot{\varepsilon}_2)|$) with increasing CCDP pass number for the UFG Al–5Mg alloy was calculated from Eq. (6) by utilizing the experimentally measured $\Delta\sigma_i(up)$ and $\Delta\sigma_i(down)$ shown in Fig. 6d. The results are denoted in Fig. 8a by square symbols. Obviously, with progressing CCDP, the asymmetry of $\Delta\sigma_i$ (or $|\sigma'_{DSA}(\dot{\varepsilon}_1) + \sigma'_{DSA}(\dot{\varepsilon}_2)|$) rose monotonically. This suggests that severe plastic deformation promotes the pinning effect (or DSA) of solute atoms. The asymmetry of $\Delta\sigma_i$ also caused an asymmetry of m_i for rate-up and rate-down jumps (Fig. 6b and d).

It is commonly accepted that σ_{DSA} increases with aging time t_a at a given $\dot{\varepsilon}$ [21,40], i.e. the longer the ageing, the larger $\sigma_{DSA}(t_a)$. This is attributed to the increasing binding
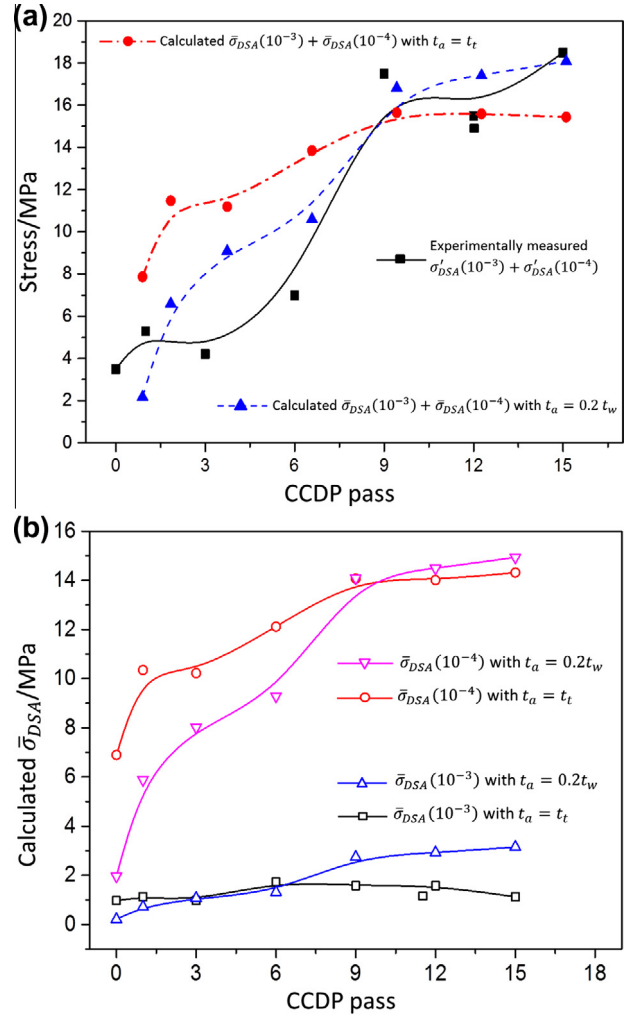

Fig. 8. Development of σ_{DSA} with progressing CCDP for Al–5Mg. (a) $\sigma_{DSA}(10^{-4}\,\mathrm{s}^{-1}) + \sigma_{DSA}(10^{-3}\,\mathrm{s}^{-1})$ obtained by experiments (squares) and model calculations with $t_a = 0.2t_w$ (triangles) and $t_a = t_t$ (circles). (b) Calculated σ_{DSA} at the strain rates of $1 \times 10^{-4}\,\mathrm{s}^{-1}$ and $1 \times 10^{-3}\,\mathrm{s}^{-1}$ with $t_a = 0.2t_w$ and $t_a = t_t$, respectively.

energy between mobile dislocations and obstacles as a longer t_a enables more solutes to diffuse to the obstacles, which, in turn, enhances the pinning effect of mobile dislocations. A direct measurement of t_a is difficult. However, the transient time, t_t, measured from strain rate-jump tests sheds light on the kinetics of DSA, since t_t is related to t_a by $t_a \propto t_t$ when $m_s < 0$ [20]. Assuming that t_t and t_a are of the same order of magnitude, i.e. $t_t \approx t_a$, and that t_a depends only on the strain rate after the rate jump, then the asymmetries of $\Delta\sigma_i$ and m_i follow from the asymmetry of t_t as confirmed by measurements (Fig. 6).

The aging time t_a also relates to the waiting time t_w of mobile dislocations in front of obstacles until the next activation event happens. During t_w DSA proceeds and thus, t_w is also an indicator of DSA kinetics, generally, $t_a \leqslant t_w$. Kubin and Estrin [12] related the mean waiting time $\bar{t}_w$ to $\dot{\varepsilon}$ by introducing the elementary strain $\Omega(\varepsilon) = b\rho_m\rho_f^{-1/2}$, a strain dependent quantity that corresponds to the deformation attained when all mobile dislocations accomplish a successful activation event, where b is Burgers vector, ρ_m and ρ_f are the mobile and the forest dislocation density, respectively, i.e.

$$\bar{t}_w = \frac{\Omega}{\dot{\varepsilon}} = \frac{b\rho_m\rho_f^{-1/2}}{\dot{\varepsilon}} = \frac{b\rho_m l_f}{\dot{\varepsilon}} \tag{7}$$

In Eq. (7), $l_f = \rho_f^{-1/2}$ is the mean spacing of forest dislocations. It can be considered as activation length or obstacle spacing, and it is related to the activation volume V^* by [41]

$$V^* = l_f \cdot b \cdot \xi \approx l_f \cdot b^2 \tag{8}$$

Here ξ is the distance swept by a glide dislocation during one activation event. On the other hand, the activation volume can be written as $V^* = kT/m_i$, where k and T are Boltzmann constant and absolute temperature, respectively. If it is assumed that $\rho_m \approx \frac{1}{3}\rho_f$ [12], then Eq. (7) can be rewritten as

$$\bar{t}_w \approx \frac{m_i b^3}{3kT\dot{\varepsilon}} \tag{9}$$

According to Eq. (9), $\bar{t}_w$ increases with m_i and decreases with rising $\dot{\varepsilon}$, i.e. during CCDP the mean waiting time $\bar{t}_w$ of mobile dislocations is obviously increased due to the enhancement of m_i owing to an increased forest dislocation density and strong grain refinement.

Soare and Curtin proposed a model for $\sigma_{DSA}(t)$ by relating the dislocation-obstacle binding energy generated by DSA to cross core diffusion [22],

$$\sigma_{DSA}(t) = \sigma_{DSA}^\infty \left(1 - \exp\left(-\left(\frac{t}{t_d}\right)^n\right)\right) \tag{10}$$

where σ_{DSA}^∞ is the saturated σ_{DSA} stress due to full aging, t_d is the characteristic time of cross-core diffusion, and $n \leqslant 1$. For evaluating σ_{DSA} in the present study, a modification was made to Eq. (10) where the time t was replaced by the aging time t_a and $n = 1$ was used in order to simplify

the calculation, and more important, to relate the $\sigma_{DSA}(t_a)$ to m_i and then to SPD strain and grain refinement (see Eqs. (8), (9)), i.e.

$$\sigma_{DSA}(t_a) = \sigma_{DSA}^\infty \left(1 - \exp\left(-\frac{t_a}{t_d}\right)\right) \tag{11}$$

By integrating Eq. (11) in the interval of $t \in [0, t_a]$, one obtains

$$\bar{\sigma}_{DSA} = \frac{\int_0^{t_a} \sigma_{DSA}^\infty \left(1 - \exp\left(-\frac{t_a}{t_d}\right)\right) dt}{t_a} \tag{12}$$

where the mean value $\bar{\sigma}_{DSA}$ during t_a is used to represent the mean DSA effect.

The average values $\bar{\sigma}_{DSA}$ of Al–5Mg were calculated for $\dot{\varepsilon} = 1 \times 10^{-4}$ s^{-1} and $\dot{\varepsilon} = 1 \times 10^{-3}$ s^{-1} by using $t_a = 0.2t_w$ and $t_a = t_t$, respectively, while t_w was determined from Eq. (9) with experimentally measured m_i. The time t_t was taken from the experimental results shown in Fig. 6c and e. The parameters σ_{DSA}^∞ and t_d in Eq. (12) used for the calculation were adopted from Ref. [22], i.e. for Al–Mg alloys $\sigma_{DSA}^\infty \cong 0.1\sigma_0$ where σ_0 is the zero temperature strength at 5% of Mg content and estimated to be 210 MPa, thus, $\sigma_{DSA}^\infty \cong 21$ MPa, and $t_d \approx 6.3$ s for cross core diffusion of Mg in Al. The calculated results are given in Fig. 8a as a function of CCDP pass number in the form of $\left|\bar{\sigma}_{DSA}(10^{-4}/s) + \bar{\sigma}_{DSA}(10^{-3}/s)\right|$. It is noted that both experimentally measured effective σ'_{DSA} at the moment of strain rate change and calculated mean values of $\bar{\sigma}_{DSA}$ at a certain strain rate follow basically a similar trend with progressing CCDP. Both σ'_{DSA} and $\bar{\sigma}_{DSA}$ lie also in a similar order of magnitude, despite their discrepancy during the first 6 CCDP passes. The reason for the discrepancy was attributed to the inhomogeneous microstructure developed during first 6 passes of CCDP. It comprised not only a distinct dislocation cell structure with a high dislocation density but also an increasing fraction of subgrains and even grains with lower dislocation density. Such microstructural inhomogeneities exert a complex influence on DSA, in particular on t_w and t_a. During late stages of CCDP with extremely high SPD strain, e.g. after 9 passes, the microstructure assumed a quasi-steady state with equiaxed subgrains/grains and hence imposed a much lower influence on t_a and t_w. Accordingly, experimental and theoretical results showed better agreement.

The $\bar{\sigma}_{DSA}$ at $\dot{\varepsilon} = 1 \times 10^{-4}$ s^{-1} and $\dot{\varepsilon} = 1 \times 10^{-3}$ s^{-1} were also calculated by Eq. (12) with $t_a = 0.2t_w$ and $t_a = t_t$, respectively, for increasing CCDP strain (Fig. 8b). Apparently, the smaller $\dot{\varepsilon}$, the larger σ_{DSA}. Also, the influence of SPD on DSA of UFG Al–5Mg was remarkably intensified by a decreasing $\dot{\varepsilon}$ (Fig. 8b).

4.3. Strain rate sensitivity

In an alloy with DSA effect, the steady state SRS, m_s measured by strain rate jump tests, can be expressed by [12,20]

$$m_s = m_i + m_{DSA} \qquad\qquad (13)$$

$$\text{or} \quad m_{DSA} = m_s - m_i \qquad\qquad (13a)$$

In Eq. (13), the instantaneous SRS is always positive, i.e. $m_i = \Delta\sigma_i/\Delta ln\dot{\varepsilon} > 0$, and the contribution of DSA to the SRS is always negative, i.e. $m_{DSA} = \Delta\sigma_{DSA}/\Delta ln\,\dot{\varepsilon} < 0$. Therefore, the competition between m_i and m_{DSA} determines the value of m_s which is a measure for the stability of plastic deformation. If $m_s \geqslant 0$, stable plastic flow will occur, but if $m_s < 0$, serrated flow will take place, and furthermore, the more negative m_s, the stronger the serrated flow or the larger the stress drop (σ_{drop}).

By using both Eq. (13a) and the experimentally measured values of m_i and m_s (Figs. 6 and 7), the changes of $\bar{m}_{DSA}$ during CCDP could be determined (Fig. 9) together with $\bar{m}_i$ and $\bar{m}_s$. Only the results of Al–5Mg are given in Fig. 9. The other alloys with lower Mg-contents showed a similar but weaker evolution profile.

It is seen that on the one hand, m_i increases monotonically with increasing strain. This can be attributed to the strong grain refinement down to the submicron/nanometer regime and an increased dislocation density, as indicated by a model prediction for UFG/NC fcc metals and alloys in [41]. On the other hand, σ_{DSA} also increased monotonically with progressing CCDP (Fig. 8), indicating an even more pronounced aging effect in UFG Al–Mg alloys and thus, a more negative m_{DSA} is expected with increasing strain, as evident from Fig. 9. However, the evolutions of m_i and m_{DSA} are different: m_i increased slowly during the first 6 passes and accelerated thereafter, by contrast, m_{DSA} changed rapidly during the first 3 passes after which its rate of change slowed down, as evidenced from the different slopes of m_i and m_{DSA} vs. SPD progress (Fig. 9). These differences caused the saddle-shaped dependency of m_s on SPD strain. It is attributed to the microstructure developed during CCDP in UFG Al–Mg alloys that exerted different

influences on m_i and m_{DSA}: at low SPD strain, e.g. below 3 to 6 CCDP passes, the microstructure was mainly comprised of cellular dislocation structures with thick cell walls. However, after 6 to 9 passes, the fraction of cells was largely reduced due to dynamic recovery and the cellular structures evolved into subgrains/grains, with increasing grain boundary volume fraction owing to the strong continuous grain refinement. Despite of the fact that both cell walls and subgrain/grain boundaries obstruct mobile dislocations, they differentiate themselves by different mechanisms. Although cell walls with high forest dislocation density strongly hinder the motion of mobile dislocation, they can be penetrated eventually [42], which is crucial for DSA to take place. Thus, an enhanced DSA effect with more negative m_{DSA} is expected during the first passes of CCDP when the fraction of cell boundaries increases. However, a cell structure does not influence m_i as much as m_{DSA} because the penetration of cell walls by mobile dislocation occurs primarily by cutting of forest dislocations, which is relatively rate-insensitive for fcc metals [43]. In contrast to cell walls, GBs are impenetrable obstacles for mobile dislocations. At high CCDP passes, due to an increased grain boundary volume fraction, the contributions of GB deformation mechanisms (e.g. GB sliding [44]) to plastic deformation become more pronounced and increase m_i effectively owing to the strongly reduced activation volume. Although pile-ups of mobile dislocations in front of GBs might enhance aging, such arrangement remains static rather than dynamic and thus, is less rate-sensitive, resulting in a slow rate of change of m_{DSA} with progressing strain. In essence, in the light of a different evolution of m_i and m_{DSA} with strain, the saddle-shaped curve of m_s vs. strain can be accounted for. Moreover, the stronger DSA effect with growing SPD strain increased the asymmetric instantaneous stress response at the strain rate change and therefore, increased the difference of the instantaneous SRS (m_i) between up and down jumps (see Fig. 6).

4.4. Influence of SPD on critical strain ε_c

In the current study it was found that the critical strain ε_c of UFG Al–Mg alloys increased with SPD strain ε and Mg content C_0 at a certain strain rate (see Fig. 5). The former is similar to observation on a coarse grained (CG) Au–Cu alloy and was attributed to strain enhanced diffusion and thus, to increased solute concentration and pinning stress at arrested dislocations, making serrated flow to occur at larger strain under higher flow stresses [6]. This interpretation in principle also holds for UFG Al–Mg alloys subjected to CCDP in the current study, as discussed in the previous sections. However, the latter behavior just opposite to CG Au–Cu alloys where ε_c decreased with rising solute content C_0 [5].

McCormick proposed a relation between the critical strain ε_c and the DSA-related parameters, such as r_{sol}, $\dot{\varepsilon}$, and Q_m, [40],
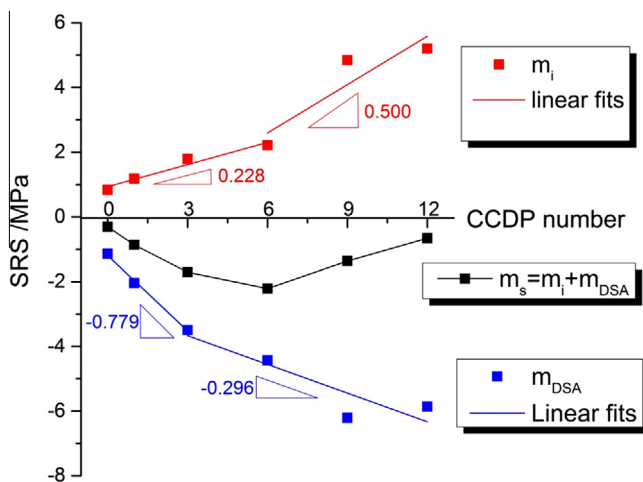

Fig. 9. Evolution of SRS in terms of m_i, m_s, and m_{DSA} with progressing CCDP for Al–5Mg as calculated from Eq. (13) with experimentally measured data.

$$\varepsilon_c^{\alpha+\beta} = \frac{r_{sol}\dot{\varepsilon}\exp(Q_m/kT)}{4bKND_0} = Ar_{sol}\dot{\varepsilon}\exp(Q_m/kT) \quad (15)$$

In Eq. (15), $r_{sol} = \Delta Eb/kT$ is the effective radius of the solute atmosphere in which ΔE is the solute-dislocation binding energy, and b is the Burgers vector, D_0 the diffusion prefactor, Q_m the effective activation energy for solute migration. K and N are the factors to link vacancy concentration C_v and dislocation density ρ to the strain ε by $C_v = K\varepsilon^\alpha$ and $\rho = N\varepsilon^\beta$ with $K \approx 10^{-4}$ and $N \approx 10^{11}$ and thus, $A = (4bKND_0)^{-1}$ is a material constant. The exponent $(\alpha + \beta) \approx 1.6 - 3.3$ for CG Al alloys [40]. From Eq. (15) it is seen that ε_c will grow, when $\dot{\varepsilon}$, Q_m and ΔE increase.

For exploring the influence of CCDP on ε_c in UFG Al–Mg alloys, Eq. (15) is modified such that the solute migration energy Q_m is replaced by the binding energy $\Delta E(t_a)$ between dislocation core and a solute atom, which is a function of aging time t_a [21,22]. This is justified since Eq. [15] originated from $\dot{\varepsilon} = \frac{4b\rho C_v D_0 \exp\left(-\frac{Q_m}{kT}\right)}{l}$ [40] that is basically a classical Arrhenius expression of $\dot{\varepsilon} = \dot{\varepsilon}_0 \exp\left(-\frac{Q(\sigma)}{kT}\right)$. In the Arrhenius expression, $Q(\sigma)$ is the activation energy that is necessary for a mobile dislocation to overcome obstacles on its glide plane. In the case of current study, where the material was a highly deformed solid solution, i.e. both solutes and forest dislocations are the main obstacles for dislocation motion. Hence, it is reasonable to write $Q(\sigma)$ as the sum of the binding energy $\Delta E(t_a)$ and $\Delta Q(f)$ needed for cut through the dislocation forest. Since the activation energy for dislocation intersection remains constant, the Arrhenius expression can be rewritten as $\dot{\varepsilon} = B\dot{\varepsilon}_0 \exp\left(-\frac{\Delta E(t_a)}{kT}\right)$ for the current study with B being a parameter that is related to its counterpart for dislocation intersection. A similar treatment has also been adopted in [21,22]. Moreover, in the modified model the influence of solute aging concentration on the critical strain was also considered by introducing a term defined by the product of solute aging concentration $C(t_a, C_0)$ and solute atom radius r'_{sol} which is a function of t_a (and also CCDP strain and grain refinement, as indicated by Eq. (9)) and alloy composition C_0, respectively. $\Delta E(t_a)$ and $C(t_a, C_0)$ can be expressed as $\Delta E(t_a) = \Delta E_\infty^{core}[1 - \exp(-t_a/t_d)]$ and $C(t_a, C_0) = C_\infty\{1 - \exp[-(C_0/C_\infty)(t_a/t_d)^n]\}$. Here ΔE_∞^{core} and C_∞ are binding energy and concentration in a fully aged state, respectively, and t_d the intrinsic cross core diffusion time, according to Curtin et al. [21]. Substituting $\Delta E(t_a)$ and $C(t_a, C_0)r'_{sol}$ into Eq. (15) yields

$$\varepsilon_c^{\alpha+\beta} = AC(t_a, C_0)r'_{sol}\dot{\varepsilon}\exp\left(\frac{\Delta E(t_a)}{kT}\right)$$

$$= A\dot{\varepsilon}r'_{sol}\left\{C_\infty\left\{1 - \exp\left[-\left(\frac{C_0}{C_\infty}\right)\left(\frac{t_a}{t_d}\right)^n\right]\right\}\right\}\exp\left\{\frac{\Delta E_\infty^{core}\left[1 - \exp\left(-\frac{t_a}{t_d}\right)\right]}{kT}\right\}$$

$$(16)$$

Eq. (16) reflects qualitatively the influences of SPD and alloy composition C_0 on ε_c of UFG Al–Mg alloys during CCDP. With increasing CCDP pass numbers, t_t and thus,
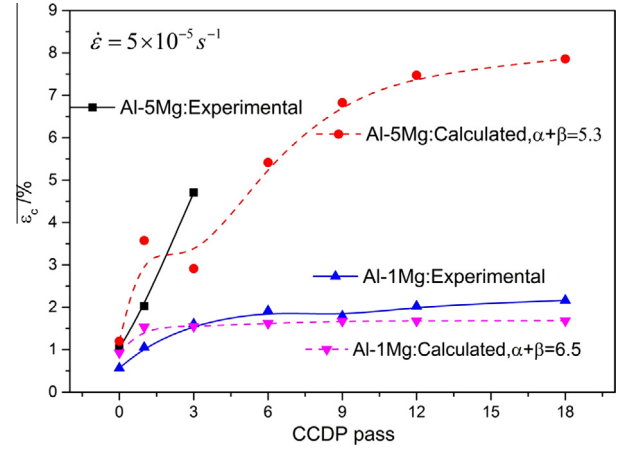

Fig. 10. Development of critical strain of Al–1Mg and Al–5Mg alloys measured by experiment and calculated from Eq. (17). Curves represent fits by 2nd order polynomials.

t_a will become larger which leads to an increase of binding energy $\Delta E(t_a)$ and solute aging concentration $C(t_a, C_0)$. Consequently, ε_c will grow with increasing CCDP pass number. Moreover, an increasing C_0 will also enlarge ε_c, as observed in the current study and expressed by Eq. (16).

The change of critical strain of Al–1Mg and Al–5Mg during CCDP was calculated by Eq. (17), with $D_0 \approx 10^{-5}$ m^2 s^{-1} and $D_0 \approx 10^{-6}$m^2 s^{-1} for CG and UFG Al–Mg alloys, respectively [45], $C_\infty \approx 10C_0$ was adopted, $r'_{sol} = 160$ pm for Mg, $t_a = t_t$ and $t_d = 6.3$ s [22]. With $\Delta E_\infty^{core} \cong 0.004$ eV/Å for each 1% of Mg and dislocation core width $\bar{w} \approx 7.5b = 21$ Å [21] ΔE_∞^{core} was calculated to be about 0.42 eV for Al–5Mg and about 0.084 eV for Al–1Mg. The calculated values of ε_c for Al–1Mg and Al–5Mg as function of CCDP pass number are given in Fig. 10 together with experimentally measured ones. Both experimentally measured and calculated results show a good agreement. The larger exponent $(\alpha + \beta)$ of ε_c used in the calculation, i.e. about $5.3 \leqslant (\alpha + \beta) \leqslant 6.5$ compared to $1.6 \leqslant (\alpha + \beta) \leqslant 3.3$ for CG Al–Mg alloys [40], is considered to be due to a larger density of vacancies and dislocations in UFG Al–Mg alloys subjected to CCDP.

5. Conclusions

The influence of severe plastic deformation (SPD) on dynamic strain aging (DSA) of Al–Mg alloys was investigated. It was found that SPD substantially influenced DSA of Al–Mg alloys.

1. DSA caused an asymmetrical instantaneous response of flow stress and strain rate sensitivity during strain rate jump tests. Such asymmetry was strongly enlarged by SPD.
2. SPD significantly intensified the DSA effect of Al–Mg alloys owing to a longer waiting time t_w and aging time t_a of dislocations arrested at obstacles, increased pinning stress σ_{DSA} exerted by aging solute atoms, and enlarged absolute value of the

DSA-related strain rate sensitivity m_{DSA}. Such effects grew considerably with increasing Mg-content. As a result, the onset of serrated flow (or critical strain ε_c) was postponed with progressing SPD and increasing Mg content. Besides, ε_c exhibited a normal relationship with respect to the strain rate for 10^{-5} s$^{-1} \leqslant \dot{\varepsilon} \leqslant 10^{-3}$ s^{-1}, and no inverse behavior of ε_c was observed in the current investigation.

3. The influence of SPD on DSA of Al–Mg alloys can be attributed to larger mobile and forest dislocation densities as well as an obviously refined grain size caused by SPD which decreased the obstacle spacing, increased the obstacle density and intensified the DSA effect by amplifying serrated flow and by retarding the onset of serrated flow.

Acknowledgment

References

[1] Cottrell AH. Phila Mag 1953;44:3.
[2] Cottrell AH, Bilby BA. Proc Phys Soc 1948;62:14.
[3] Curtin WA, Olmsted DL, Hector LG. Nat Mater 2006;5:875.
[4] Van den Beukel A, Kocks UF. Acta Metall 1982;30:1027.
[5] Van den Brink SH, Van den Beukel A, McCormick PG. Phys Status Solidi A 1975;30:469.
[6] Van den Beukel A. Phys Status Solidi A 1975;30:197.
[7] Van den Beukel A. Acta Metall 1980;28:965.
[8] Kocks UF, Cook RE, Mulford RA. Acta Metall 1985;33:623.
[9] Mulford RA, Kocks UF. Scr Metall 1979;13:729.
[10] Wycliffe P, Kocks UF, Embury JD. Scr Metall 1980;14:1349.
[11] Sleeswyk AW. Acta Metall 1958;6:598.
[12] Kubin LP, Estrin Y. Acta Metall Mater 1990;38:697.
[13] Brechet Y, Estrin Y. Acta Metall Mater 1995;43:955.
[14] Kubin LP, Chihab K, Estrin Y. Acta Metall 1988;36:2707.
[15] Kubin LP, Estrin Y, Perrier C. Acta Metall Mater 1992;40:1037.
[16] Balik J, Lukac P. Acta Metall Mater 1993;41:1447.
[17] Balik J. Mater Sci Eng, A 2001;316:102.
[18] Hähner P, Rizzi E. Acta Mater 2003;51:3385.
[19] Rizzi E, Hähner P. Int J Plast 2004;20:121.
[20] Hähner P. Acta Mater 1997;45:3695.
[21] Soare MA, Curtin WA. Acta Mater 2008;56:4091.
[22] Soare MA, Curtin WA. Acta Mater 2008;56:4046.
[23] Picu RC. Acta Mater 2004;52:3447.
[24] Picu RC, Vincze G, Ozturk F, Gracio JJ, Barlat F, Maniatty AM. Mater Sci Eng, A 2005;390:334.
[25] Picu RC, Zhang D. Acta Mater 2004;52:161.
[26] Fu S, Cheng T, Zhang Q, Hu Q, Cao P. Acta Mater 2012;60:6650.
[27] Cai MC, Niu LS, Yu T, Shi HJ, Ma XF. Mater Sci Eng, A 2010;527:5157.
[28] Kapoor R, Chakravartty JK. Acta Mater 2007;55:5408.
[29] Kapoor R, Gupta C, Sharma G, Chakravartty JK. Scripta Mater 2005;53:1389.
[30] Blum W, Li YJ, Breutinger F. Mater Sci Eng, A 2007;462:275.
[31] Zhang S, Hu W, Berghammer R, Gottstein G. Acta Mater 2010;58:6695.
[32] Zhang S. [Master Thesis]. RWTH Aachen University; 2010.
[33] Hughes DA. Acta Metall Mater 1993;41:1421.
[34] Gubicaza J, Chinh NQ, Horita Z, Langdon TG. Mater Sci Eng, A 2004;387–389:55.
[35] Morris DG, Morris MA. Acta Mater 2002;50:4047.
[36] Hayes RW, Witkin D, Zhou F, Lavernia EJ. Acta Mater 2004;52:4259.
[37] Witkin D, Han BQ, Lavernia EJ. Metall Mater Trans A 2006;37A:185.
[38] Han BQ, Huang J, Zhu YT, Lavernia EJ. Adv Eng Mater 2006;8:945.
[39] Rupert TJ, Trenkle JC, Schuh CA. Acta Mater 2011;59:1619.
[40] McCormic PG. Acta Metall 1972;20:351.
[41] Wei Q, Cheng S, Ramesh KT, Ma E. Mater Sci Eng, A 2004;381:71.
[42] Roters F, Raabe D, Gottstein G. Acta Mater 2000;48:4181.
[43] Gottstein G. Physical foundations of materials science. 2nd ed. Berlin: Springer; 2004.
[44] Meyers M, Mishra A, Benson D. Prog Mater Sci 2006;51:427.
[45] Fujita T, Horita Z, Langdon TG. Mater Sci Eng, A 2004;371:241.